J. Fluid Mech. (2004), *vol.* 507, *pp.* 265–288.
DOI: 10.1017/S002211200400864X Printed in the United Kingdom

Mode competition between rotating waves in a swirling flow with reflection symmetry

By J. M. LOPEZ[1] AND F. MARQUES[2]

[1]Department of Mathematics and Statistics, Arizona State University, Tempe, AZ 85287, USA

[2]Departament de Física Aplicada, Universitat Politècnica de Catalunya, 08034, Barcelona, Spain

(Received 15 July 2003 and in revised form 15 December 2003)

Flow in a cylinder driven by the co-rotation of the top and bottom endwalls displays distinct instability mechanisms, depending on whether its aspect ratio (length to diameter) is large or small. When the cylinder length is about the same as its diameter, the two mechanisms compete and lead to a stable mixed mode solution. Using numerical computations of the three-dimensional Navier–Stokes equations, together with equivariant bifurcation and normal form theory, we explore the nature of this mode competition, both from a flow physics point of view and from a dynamical systems with symmetry point of view. The results help to clarify the distinct behaviours observed experimentally in some short and long cylinder flows.

1. Introduction

Systems with nominally flat clean surfaces are often modelled as being stress free, and this stress-free interface is essentially equivalent to a reflection symmetry plane. However, it is practically impossible to attain a perfectly stress-free interface, particularly in an air/water system, because of the ubiquitous presence of surfactants (Scott 1975) whose surface concentration gradients produce a Marangoni stress. There has been recent interest in flows in open cylindrical containers driven by the rotation of the bottom endwall, and the various instability modes of such flows (Spohn 1991; Spohn, Mory & Hopfinger 1993; Young, Sheen & Hwu 1995; Spohn, Mory & Hopfinger 1998; Hirsa, Lopez & Miraghaie 2002; Miraghaie, Lopez & Hirsa 2003). Modelling efforts in these flows have typically approached the problem by imposing the reflection symmetry (Valentine & Jahnke 1994; Lopez 1995; Gelfgat, Bar-Yoseph & Solan 1996; Brons, Voigt & Sorensen 1999, 2001). For deep systems ($H > R$, where H is the depth from the free surface to the bottom endwall and R is the cylinder radius), the stress-free surface model works quite well in describing the primary mode of instability, which is non-axisymmetric (Hirsa *et al.* 2002; Lopez *et al.* 2004). However, for shallow systems ($R > H$), the model is incapable of describing the primary mode of instability. In this case, the primary mode corresponds to a spontaneous breaking of the reflection symmetry (Miraghaie *et al.* 2003; Lopez *et al.* 2004). For systems with $R \sim H$, the two primary modes of instability (Z_2-reflection preserving for deep systems and Z_2-reflection breaking for shallow systems) compete, and it is this competition that is explored here in a closed system with both the top and bottom endwalls rotating, so that the basic state has a Z_2-symmetric mid-plane modelling the stress-free interface.

The symmetry $Z_2 \times SO(2)$ (where in the problem we address here, the Z_2 is a reflection about $z = 0$ and $SO(2)$ is invariance to rotations about the axis $r = 0$) plays

a role in many fluids problems. Classic examples are Taylor–Couette flow in physical containers, i.e. with endwalls and of finite length (Benjamin 1978; Benjamin & Mullin 1981; Cliffe & Mullin 1985; Cliffe, Kobine & Mullin 1992; Mullin, Toya & Tavener 2002; Schulz, Pfister & Tavener 2003), and Rayleigh–Bénard convection in rotating cylinders (Zhong, Ecke & Steinberg 1991; Goldstein *et al.* 1993, 1994). The role of Z_2-symmetry breaking has attracted much attention, particularly in the Taylor–Couette flows, but the focus has typically been on steady-state Z_2-symmetry breaking (via a pitchfork bifurcation) and the theoretical and numerical studies have been restricted mainly to $SO(2)$ invariant subspaces, i.e. axisymmetric flows. Symmetry-breaking Hopf bifurcations, such as those examined here, have received comparatively little attention. A fundamental difference is that the Z_2-symmetry breaking Hopf bifurcation leads to another single state – a Z_2-symmetric limit cycle which is not pointwise Z_2-symmetric, but rather it is setwise Z_2-symmetric (e.g. see Golubitsky, Stewart & Schaeffer 1988). The interaction and competition between Z_2-symmetry preserving and Z_2-symmetry breaking Hopf bifurcations is explored in detail here, both by examining a full fluid dynamics problem and in terms of its centre manifold reduction and normal form analysis of the corresponding double Hopf bifurcation. The main result is the existence of a stable mixed mode. Nore *et al.* (2003) have studied a related problem, swirling flow in a stationary cylinder driven by the exact counter-rotation of the endwalls. Their symmetry is different, $O(2)$ that mixes the axial and azimuthal directions z and θ, but again competition between distinct instability modes led to a mixed mode, whose normal form dynamics were predicted in Armbruster, Guckenheimer & Holmes (1988).

In Lopez & Marques (2003), a Taylor–Couette flow with $SO(2) \times Z_2$ symmetry also displayed mode competition organized by a double Hopf bifurcation, but in that case the competition was between an axisymmetric ($m = 0$) limit cycle and a rotating wave with azimuthal wavenumber $m = 1$. Since one of the limit cycles had wavenumber $m = 0$, the mode competition was non-resonant (Marques, Lopez & Shen 2002). Furthermore, in the mode competition parameter regime, the two limit cycles co-existed and were stable, while the mixed mode was unstable. In our present problem, the mode competition is between two rotating waves with $m = 1$ and $m = 2$, and so resonance may be a factor in the dynamics. Here, we derive the equivariant double Hopf normal form and the conditions for resonance, and show that, in fact, our problem is non-resonant. A distinction between the present mode competition and that in Lopez & Marques (2003) is that here the mixed mode is stable, and the two limit cycles (rotating waves) are unstable. The stability of the mixed mode allows a comprehensive description of its spatiotemporal characteristics.

2. Governing equations, symmetries and numerical method

We consider the flow in a cylinder of length $2H$ and radius R, driven by the co-rotation of both rigid endwalls at constant angular speed Ω, as shown in figure 1. Using R as the length scale and $1/\Omega$ as the time scale, there are two non-dimensional governing parameters:

$$\text{Reynolds number:} \quad Re = \Omega R^2/\nu,$$
$$\text{Aspect ratio:} \quad \Gamma = H/R,$$

where ν is the kinematic viscosity of the fluid.

The equations governing the flow are the Navier–Stokes equations together with initial and boundary conditions. In cylindrical coordinates, the domain is $(r, \theta, z) \in [0, 1] \times [0, 2\pi] \times [-\Gamma, \Gamma]$, and the non-dimensional velocity vector is $\boldsymbol{u} = (u, v, w)$. The

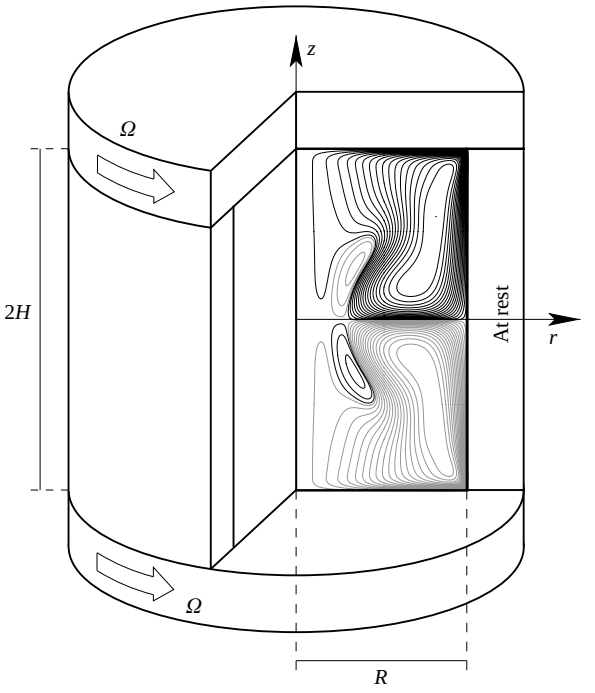

FIGURE 1. Schematic of the flow apparatus. The inset illustrates typical streamlines of a steady axisymmetric flow determined by numerical simulation, projected onto a meridional plane.

boundary conditions are no-slip for all solid walls and the *essential* pole conditions at the axis; see Lopez, Marques & Shen (2002) for details, where the treatment of the discontinuity at $(r=1, z=\pm\Gamma)$ is also discussed.

The three-dimensional Navier–Stokes equations are solved numerically using a Galerkin spectral scheme for spatial discretization and a second-order projection scheme for time-evolution. Legendre polynomial bases are used in the radial and axial directions and a Fourier basis is used in the periodic azimuthal direction. The details of the numerical method are given in Lopez *et al.* (2002). The computed results presented here employed 48 Legendre modes in r and z, 32 Fourier modes in θ, and a time step of 2×10^{-2}. The initial condition is either a state of rest or the continuation of a solution from one point in the (Re,Γ)-parameter space to a nearby point in that parameter space.

The governing equations and boundary conditions are equivariant to rotations R_β, of arbitrary angle β, around the cylinder axis, and to a reflection K about the mid-plane $z=0$. Their actions on the velocity vector $\boldsymbol{u}$ are

$$R_\beta(u, v, w)(r, \theta, z) = (u, v, w)(r, \theta+\beta, z), \tag{2.1}$$

$$K(u, v, w)(r, \theta, z) = (u, v, -w)(r, \theta, -z). \tag{2.2}$$

Since R_β and K commute, the symmetry group of the problem is $\mathcal{G}=SO(2)\times Z_2$. The basic state, i.e. the unique solution of the Navier–Stokes equations for small values of Re, is steady and invariant to the group $\mathcal{G}$.

We shall consider the dynamics in a number of invariant subspaces: (i) the $SO(2)\times Z_2$-invariant subspace, where all solutions are axisymmetric and reflection symmetric about the mid-plane $z=0$; (ii) the $SO(2)$-invariant subspace, where all solutions are

axisymmetric but the mid-plane need not be a symmetry plane; (iii) the Z_2-invariant subspace, where the mid-plane is a symmetry plane but the solutions need not be axisymmetric; and finally (iv) the full problem where no symmetry conditions are imposed. With the spectral method used, the restriction to the axisymmetric $SO(2)$-invariant subspace is accomplished by setting to zero all but the zeroth Fourier mode; the restriction to the Z_2-invariant subspace is simply accomplished by setting to zero all the odd Legendre polynomials in the z-basis for u and v and all the even Legendre polynomials in the z-basis for w. This enforces the condition

$$\partial u/\partial z = \partial v/\partial z = w = 0, \tag{2.3}$$

at the mid-plane, which means that on this plane there is no flow-through (maintaining it flat) and there are no tangential stresses. The restriction to the $SO(2) \times Z_2$-invariant subspace is accomplished by imposing both $SO(2)$ and Z_2 invariance.

3. Basic flow state

For the base flow, it is often convenient to describe the axisymmetric solutions in terms of the streamfunction, ψ, the axial component of angular momentum, α, and the azimuthal component of the vorticity, η. These are related to the velocity and vorticity fields as

$$\boldsymbol{u} = (u, v, w) = (-\psi_z, \alpha, \psi_r)/r, \tag{3.1}$$

$$\nabla \times \boldsymbol{u} = (-\alpha_z, r\eta, \alpha_r)/r. \tag{3.2}$$

In the same way as contours of ψ give the projection of the streamsurfaces onto a meridional plane (i.e. the streamlines), contours of α give the vortex lines in the meridional plane. For a Z_2-invariant state, ψ and η are odd functions of z and α is even.

Figure 2 shows the streamlines, vortex lines and lines of constant azimuthal vorticity of the basic state for $\Gamma = 1$, at $Re = 1950$, just lower than the Re for which the basic state becomes unstable. Near the axis, $r = 0$, the vortex lines are vertical straight lines, producing a region of solid-body rotation that extends to about $r = 0.2$. In a solid-body rotation region, the angular velocity $\omega = v/r = \alpha/r^2$ is constant, and α depends only on r, producing the vertical straight lines; and since α is quadratic in r, the vortex lines are equispaced for quadratically spaced contour levels. There is virtually no secondary meridional motion in this near-axis region, i.e. $\psi \to 0$ here. We have spaced the streamlines quadratically, in order to visualize the very weak recirculation bubbles near the edge of the solid-body-rotation region. The endwall boundary layers at $z = \pm\Gamma$ for $r > 0.2$ carry angular momentum to larger radii, and wall jet-shear layers form as these are turned into the interior by the presence of the stationary cylinder at $r = 1$. These jet-shear layers are inclined at a small angle in from the wall and are distinct from the cylinder wall boundary layers, which remain attached up to the mid-plane at $z = 0$. Figure 3 shows contours of the three velocity components of the same basic state as in figure 2; these contours are linearly spaced. The contours of v further illustrate the structure of the inclined wall jet-shear layers, where v has local maxima near the corners ($r = 1$, $z = \pm\Gamma/2$). At the mid-plane $z = 0$, the cylinder wall layers (coming in from $z = \pm\Gamma$) separate forming a radially inwards swirling jet at $z = 0$ that penetrates to small radii, up to the region of solid-body rotation. This jet has radial and azimuthal velocity components that are of comparable strength, as seen in the contours (figure 3). Velocity profiles plotted in figure 4 further detail the structure of the jet at the mid-plane. Figure 4(a) gives the axial profiles of the three

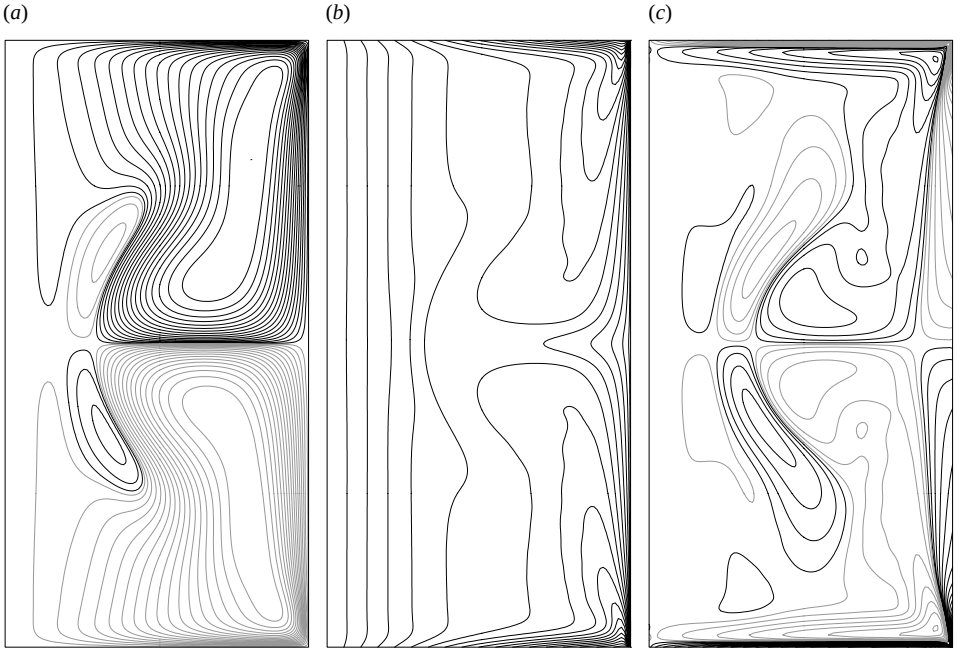

FIGURE 2. Basic state at $\Gamma = 1.0$, $Re = 1950$, showing contours of (*a*) ψ, (*b*) α and (*c*) η in a meridional plane $(r, z) \in [0, 1] \times [-\Gamma, \Gamma]$. Contour levels, 18 positive (black) and 18 negative (grey), are spaced quadratically with $\psi \in [-0.008, 0.008]$, $\alpha \in [0, 1]$, $\eta \in [-18, 18]$.

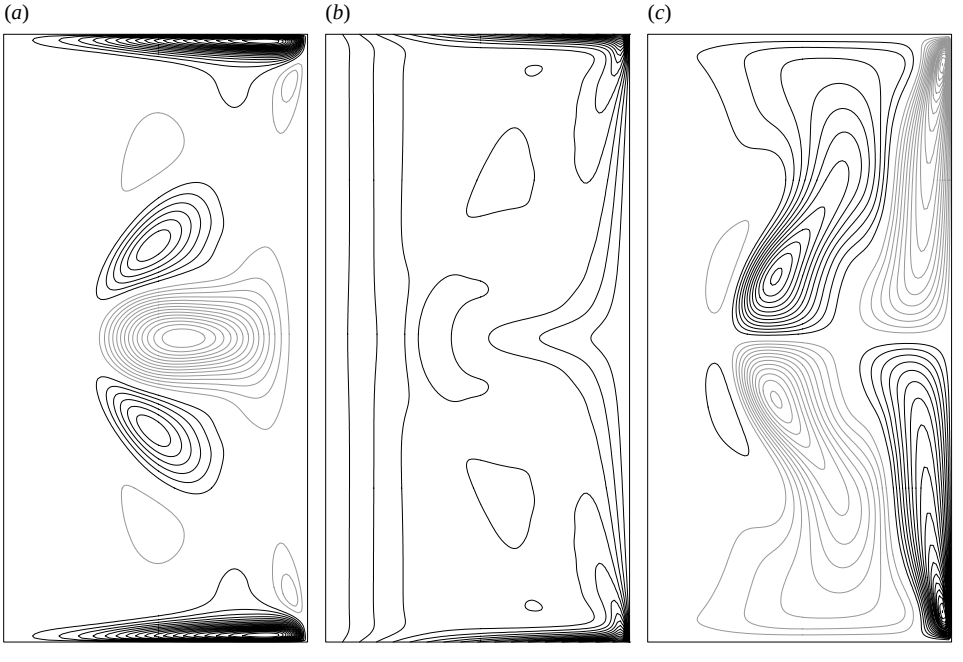

FIGURE 3. Basic state at $\Gamma = 1.0$, $Re = 1950$, showing contours of (*a*) u, (*b*) v and (*c*) w in a meridional plane $(r, z) \in [0, 1] \times [-\Gamma, \Gamma]$. Contour levels, 18 positive (black) and 18 negative (grey), are spaced linearly $u \in [-0.145, 0.145]$, $v \in [0, 1]$, $w \in [-0.132, 0.132]$.

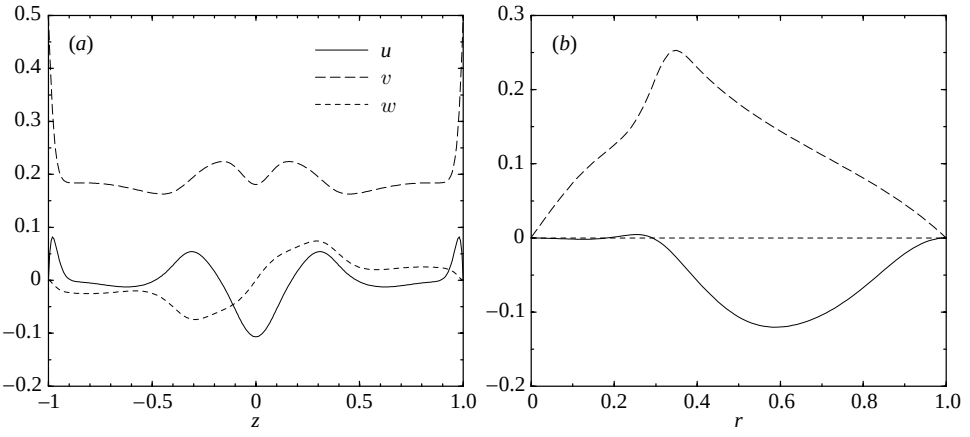

FIGURE 4. Velocity profiles of the basic state at $Re = 1950$, $\Gamma = 1.0$ in (a) the axial direction at $r = 0.5$ and (b) the radial direction at $z = 0$.

velocity components at mid-radius $r = 0.5$; the u profile shows a typical jet profile with maximum in its core and the w profile shows the convergent flow into the jet core. The jet's core extends between approximately $z = \pm 0.3\Gamma$, and all three velocity components are of comparable magnitude. Figure 4(b) gives the radial variations of the velocity components at the mid-plane, i.e. along the core of this jet. The w velocity here is zero; the basic state is Z_2 symmetric. The u profile shows that the jet extends from the sidewall all the way to the solid-body-rotation region at about $r = 0.2$. The v velocity increases linearly as it is advected by the jet from the sidewall, owing to approximate conservation of angular momentum rv, and reaches a maximum as the jet collides with the region of solid-body rotation (where v/r is approximately constant). Figure 2 shows this jet colliding with the region of solid-body rotation at about $r = 0.2$ and fluid being turned into the $\pm z$ directions. The characteristic recirculation zones attached to the mid-plane and the associated large azimuthal component of vorticity due to vortex line bending (Brown & Lopez 1990) are also clearly evident. Such recirculation zones have been visualized experimentally (Spohn *et al.* 1993), where the mid-plane in our computations corresponds to their free surface. The structure of this basic state is quite complex, it is an axisymmetric flow but has a three component velocity field, and consists of several boundary layers and internal shear layers and jets, all of which are interacting intimately.

4. Bifurcations from the basic state

4.1. *Symmetry considerations*

The primary instability of the basic state leads to a limit cycle, γ, via a Hopf bifurcation. The normal form for a Hopf bifurcation from a base state with symmetry group $\mathscr{G} = SO(2) \times Z_2$ is the same as for the standard Hopf bifurcation. Using the complex amplitude of the limit cycle, A, the normal form, up to third order in A, is

$$\dot{A} = A(\mathrm{i}\omega^0 + \mu - a|A|^2), \tag{4.1}$$

where ω^0 is the imaginary part of the critical eigenvalue at the bifurcation and μ is the bifurcation parameter (related to Re and Γ in our case). Although the presence of the symmetry group $\mathscr{G}$ does not modify the generic Hopf normal form, the bifurcated solution, γ, may have symmetries different from $\mathscr{G}$. The action of $\mathscr{G}$ on the amplitude

A is (Iooss & Adelmeyer 1998):

$$R_\beta A = \mathrm{e}^{\mathrm{i}m\beta} A, \quad KA = sA, \tag{4.2}$$

where m is an integer (the azimuthal wavenumber of γ in our problem) and $s = \pm 1$. When $m = 0$, the eigenvector is $SO(2)$-invariant, i.e. axisymmetric; when $s = +1$, the eigenvector is Z_2-invariant. The action of $\mathscr{G}$ on the periodic bifurcated solution γ is the following: if $m = 0$, the action of R_β leaves every point of γ invariant. If $m \neq 0$, the action of R_β on γ is equivalent to a time translation $t \to t + m\beta/\omega^0$: advancing in time is equivalent to a rigid rotation of the flow pattern, and γ is called a rotating wave with precession frequency $\omega_p = \omega^0/m$. If $s = 1$, the action of K leaves every point of γ invariant. If $s = -1$, the action of K is equivalent to a time translation of π/ω^0, which is half the period of γ.

The bifurcated limit cycle γ, as a set, is $\mathscr{G}$-invariant, but the individual points on γ (the solution at a given time), are only invariant to a subgroup Δ of $\mathscr{G}$, called the group of spatial symmetries of the bifurcated periodic solution. That is, applying an element of $\mathscr{G}$ to a given point in γ will either leave it invariant or produce a symmetrically related point in γ. The elements of $\mathscr{G}$ which leave the point invariant form the subgroup Δ. The remaining elements of $\mathscr{G}$ are called spatiotemporal symmetries of γ, and their action is equivalent to a specified time translation along the orbit (Lamb & Melbourne 1999). There are four different possibilities for the symmetries of the bifurcated orbit γ:

	m	s	Δ
Type I	0	$+1$	$SO(2) \times Z_2$
Type II	0	-1	$SO(2)$
Type III	$\neq 0$	$+1$	$Z_m \times Z_2$
Type IV	$\neq 0$	-1	Z_{2m}

(4.3)

where Z_m is the discrete group of rotations generated by $R_{2\pi/m}$, and Z_{2m} is generated by $KR_{\pi/m}$; the notation $Z_m(R_{2\pi/m})$ and $Z_{2m}(KR_{\pi/m})$ is often used to indicate simultaneously the group and the corresponding generator(s); Z_2 is generated by the reflection K: $Z_2(K)$.

In our problem, we have found Hopf bifurcations leading to limit cycles with symmetries corresponding to all four cases. The axisymmetric Hopf bifurcations (types I and II) have been previously studied by restricting the computations to an $SO(2)$-invariant subspace (Valentine & Jahnke 1994; Lopez 1995; Brons *et al.* 2001), but our three-dimensional computations have found that these take place at Re much larger than the Re at which the basic state undergoes non-axisymmetric Hopf bifurcations (types III and IV); compare $Re_c \sim 1960$ in the present study with $Re_c \sim 2564$ (axisymmetric Hopf bifurcation) for $\Gamma = 1$.

When the aspect ratio Γ is greater than one (deep systems), the basic state loses stability to a mode with even z-parity ($s = +1$), while in shallow systems (Γ smaller than one), the primary instability mode has odd z-parity ($s = -1$). Near $\Gamma = 1$, both modes with opposite z-parity compete, and we have located a double Hopf bifurcation point (at $\Gamma = 1.0264$ and $Re = 1949.07$) where both modes bifurcate simultaneously. This codimension-2 point is the organizing centre for the dynamics and flow physics associated with this mode competition.

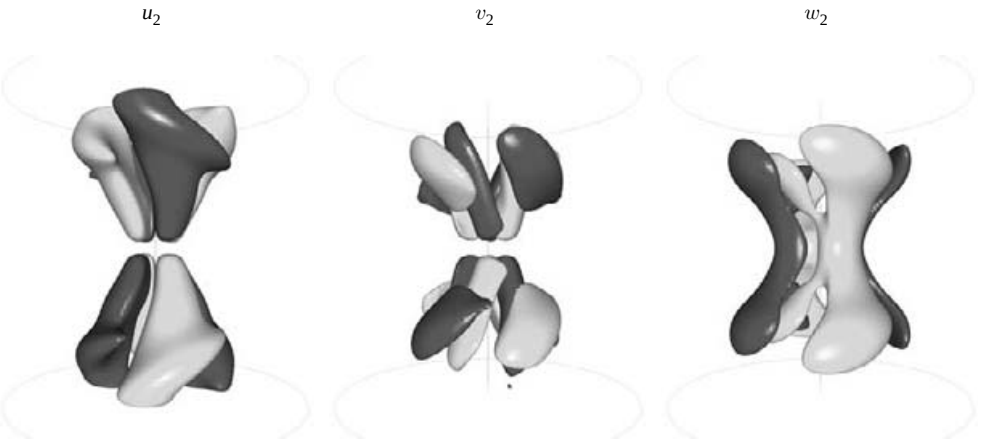

FIGURE 5. Isosurfaces of the $m=2$ velocity components of RW$_2$ with odd z-parity at $Re=2000$, $\Gamma=1.0$; isolevels at ± 0.003.

4.2. *Numerical results*

The $\Gamma=1$ case illustrates the mode competition between non-axisymmetric odd and even z-parity modes. The basic state loses stability to each of these types of mode at critical Re that are quite close. The odd z-parity mode bifurcates first in a supercritical Hopf bifurcation at $Re\approx 1955$. It has azimuthal wavenumber $m=2$ and leads to a rotating wave RW$_2$.

The structure and symmetry of the $m=2$ Fourier component of the velocity components of RW$_2$ at $Re=2000$ are shown in figure 5. The $w=0$ surface near the mid-plane $z=0$ undulates with azimuthal wavenumber $m=2$. The isosurfaces show that this Hopf mode has odd z-parity and RW$_2$ has type IV symmetry ($m=2$ and $s=-1$). According to (4.3), the spatial symmetry group of the bifurcated solution is Z_4, generated by $KR_{\pi/2}$, i.e. a reflection about $z=0$ composed with a rotation of $\pi/2$ about the axis. Figure 5 shows that u and v have this symmetry. For w it is more complicated, because the action of K also changes the sign of the vertical velocity (see (2.2)); therefore neither K nor $R_{\pi/2}$ leave w invariant, but their combination does. Neither K nor R_β are spatial symmetries of RW$_2$, but they are spatiotemporal symmetries. For K, its action is equivalent to a half-period temporal evolution, and R_β is equivalent to a temporal evolution of β/π of the period (characteristic of a rotating wave with $m=2$).

As Re is increased, the RW$_2$ with broken spatial Z_2 symmetry becomes unstable via a Neimark–Sacker bifurcation that introduces an $m=1$ component at $Re\approx 2005$ (see figure 7), leading to a modulated rotating wave MRW. Isosurfaces of the $m=1$ velocity components of MRW at $Re=2050$ are shown in figure 6. It is clear that the $m=1$ component has even z-parity.

It is interesting to compute in a Z_2-invariant subspace for $\Gamma=1$. In this subspace, the odd z-parity RW$_2$ does not exist, and neither does MRW. The first instability of the basic state in this subspace, as Re is increased, is to an $m=1$ mode at $Re\approx 2005$, leading to an even z-parity rotating wave RW$_1$. Figure 7 shows the modal energies of the RW$_1$, RW$_2$ and MRW solutions as functions of Re. The modal energies are

$$E_m=\frac{1}{2}\int_{z=-\Gamma}^{z=\Gamma}\int_{r=0}^{r=1} e_m\, r\,\mathrm{d}r\,\mathrm{d}z, \tag{4.4}$$

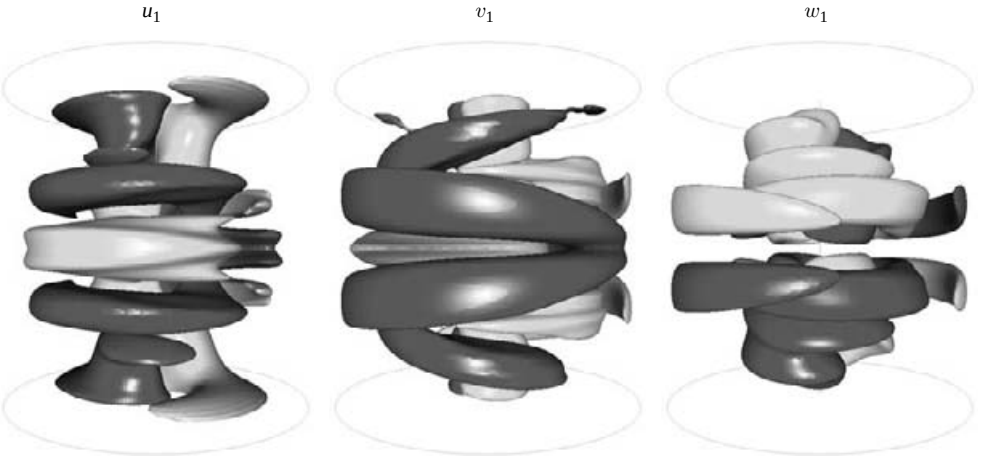

FIGURE 6. Isosurfaces of the $m = 1$ velocity components of MRW at $Re = 2050$, $\Gamma = 1.0$; isolevels at ± 0.003.

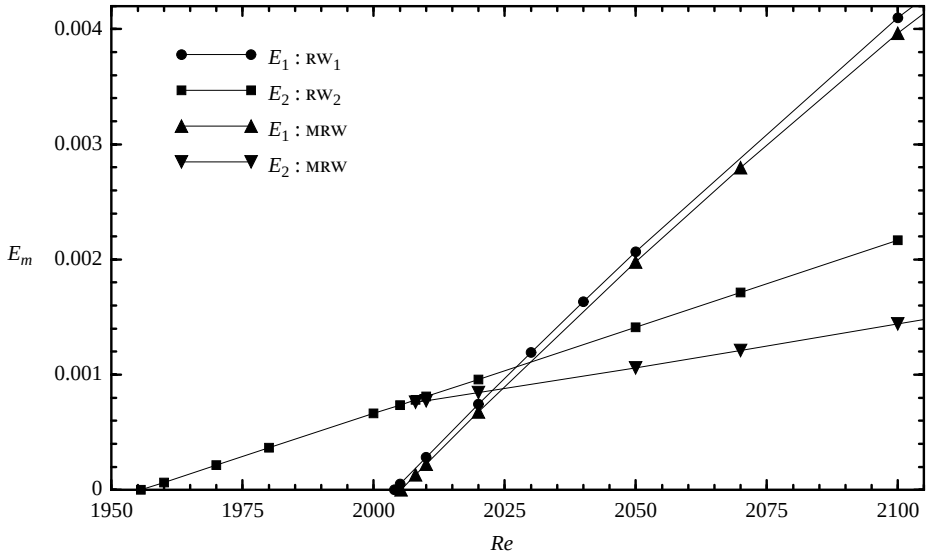

FIGURE 7. Variation with Re of E_2 for RW$_2$, E_2 and E_1 for MRW, and E_1 for RW$_1$, for $\Gamma = 1$.

where

$$e_m = \boldsymbol{u}_m \cdot \overline{\boldsymbol{u}}_m, \tag{4.5}$$

is the modal energy density and $\boldsymbol{u}_m$ is the mth Fourier mode of the velocity field. Comparing the E_1 modal energies of MRW and RW$_1$ in figure 7, we find that they are very close over an extensive range in Re, with E_1 of RW$_1$ consistently larger than that of MRW. Both modal energies, E_1 and E_2, of MRW increase with Re, but E_1 grows much faster with Re than does E_2, and by $Re \approx 2010$, the $m = 1$ component of MRW is dominant. Although the first instability of the basic state at $\Gamma = 1$ breaks the spatial Z_2 symmetry in z, the flow quickly (in terms of increasing Re) attempts to re-establish a Z_2 symmetric state, and with increasing Re the ratio E_1/E_2 increases and the flow progressively becomes more Z_2 symmetric. Figure 8 shows isosurfaces of the $m = 1$

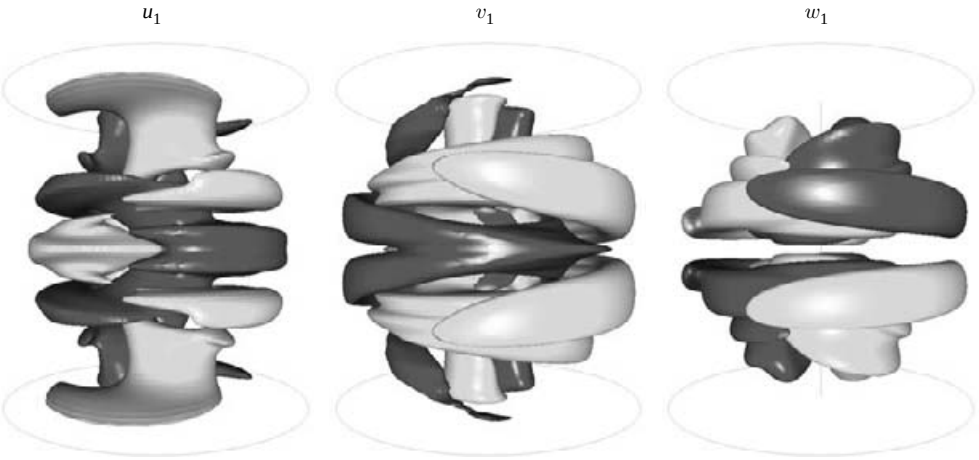

FIGURE 8. Isosurfaces of the $m = 1$ velocity components of RW$_1$ with even z-parity at $Re = 2050$, $\Gamma = 1.0$; isolevels at ± 0.003.

velocity components of RW$_1$ at $Re = 2050$ and $\Gamma = 1.0$, the same parameters as used in figure 6 for the corresponding isosurfaces of MRW; the two modes are clearly very similar. Using the RW$_1$ state as an initial condition in a computation without any imposed symmetry conditions, together with a small odd z-parity perturbation, results in an evolution with a growing $m = 2$ component and eventually the MRW state is reached. The RW$_1$ state is unstable for $\Gamma = 1.0$.

The isosurfaces in figure 8 show that RW$_1$ has even z-parity and type III symmetry ($m = 1$ and $s = +1$). According to (4.3), the spatial symmetry group of the bifurcated solution is $Z_1 \times Z_2$ which is isomorphic to Z_2 (because Z_1 is the trivial group, consisting of the identity). The Z_2 is generated by K. R_β is not a spatial symmetry of RW$_1$, but it is a spatiotemporal symmetry: its action is equivalent to a temporal evolution of $\beta/2\pi$ of the period (characteristic of a rotating wave with $m = 1$).

An interpretation of MRW as a mixed mode between the odd z-parity RW$_2$ and the even z-parity RW$_1$ is apparent. Further, given that RW$_2$ and RW$_1$ bifurcate from the basic state at quite close values of Re at $\Gamma = 1$ suggests that for a nearby value of Γ, they could bifurcate simultaneously, i.e. at a codimension-2 double Hopf bifurcation point, and that MRW is a mixed mode that originates at the bifurcation point.

A typical feature associated with double Hopf bifurcations is the existence of a mixed mode, which may be stable, depending on the particulars of the system; see detailed accounts for the generic case in, for example, Guckenheimer & Holmes (1997) or Kuznetsov (1998). When the system has symmetries, these may introduce new dynamics (Golubitsky *et al.* 1988), and before presenting further numerical results for our problem, we first determine how the symmetry group $SO(2) \times Z_2$ affects the dynamics. The details are given in the Appendix, and in the following section we present the salient points.

5. Double Hopf bifurcation with $SO(2) \times Z_2$ symmetry

In the double Hopf bifurcation, the presence of $SO(2) \times Z_2$ symmetry alters the generic normal form only in the presence of resonances. In the Appendix, we present a derivation of the normal form for the double Hopf bifurcation with $SO(2) \times Z_2$

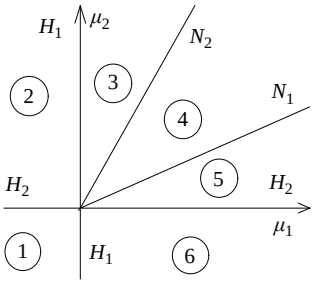

FIGURE 9. Parametric portrait for a simple type II double Hopf bifurcation. The curves H_1 and H_2 (coinciding with the axes $\mu_1 = 0$ and $\mu_2 = 0$, respectively) are the two Hopf bifurcation curves at which the limit cycles, P_1 and P_2, bifurcate supercritically from the basic state P_0. The curves N_1 and N_2 are Neimark–Sacker bifurcation curves at which the quasiperiodic mixed mode P_3 bifurcates. Phase portraits in each of the six regions indicated are shown in figure 10.

symmetry. We show that the symmetries inhibit resonances, as in the double Hopf bifurcation with $SO(2)$ symmetry in Marques *et al.* (2002). The resonance condition is $\omega_2^0/\omega_1^0 = m_2/m_1$ (ω_2^0 and ω_1^0 are the Hopf frequencies at the bifurcation), i.e. resonance is only possible if both the frequencies and the azimuthal wavenumbers are in the same ratio. In the present problem, we shall show below that our double Hopf bifurcation is far from resonance and the corresponding normal form is simply that for the generic double Hopf bifurcation. In terms of the moduli and phases of the complex amplitudes of the eigenvectors, the normal form can be written, up to fourth order, as A 20:

$$\left.\begin{aligned} \dot{r}_1 &= r_1\left(\mu_1 + p_{11}r_1^2 + p_{12}r_2^2 + q_1 r_2^4\right), \\ \dot{r}_2 &= r_2\left(\mu_2 + p_{21}r_1^2 + p_{22}r_2^2 + q_2 r_1^4\right), \\ \dot{\phi}_1 &= \omega_1^0 + \psi_1(r_1, r_2, \mu_1, \mu_2), \\ \dot{\phi}_2 &= \omega_2^0 + \psi_2(r_1, r_2, \mu_1, \mu_2), \end{aligned}\right\} \tag{5.1}$$

where μ_1 and μ_2 are the normalized bifurcation parameters and $\mu_1 = \mu_2 = 0$ at the bifurcation point. The p_{ij} and q_i depend on the parameters μ_1 and μ_2, and satisfy a non-degeneracy condition in the neighbourhood of the bifurcation, $p_{ij} \neq 0$.

The normal form (5.1) admits a multitude of distinct dynamical behaviours, depending on the values of p_{ij} and s_i. These are divided into so-called simple ($p_{11}p_{22} > 0$) and difficult ($p_{11}p_{22} < 0$) cases. In the simple cases, the topology of the bifurcation diagram is independent of the q_i terms. Even in the simple case, several different bifurcation diagrams exist. A comprehensive description of all the simple and difficult scenarios is given in Kuznetsov (1998). In our problem, the double Hopf bifurcation is of type II simple (Kuznetsov 1998).

Figure 9 shows the parametric portrait in a neighbourhood of the double Hopf bifurcation point, for the case corresponding to our problem. Parameter space is divided into six regions, delimited by bifurcation curves. The number of solutions and their stability is different in each region. Figure 10 shows typical phase portraits in these six different regions. P_1 and P_2 are rotating waves emerging from the basic state P_0 when the Hopf bifurcation curves H_1 and H_2 are crossed. There is a region (4 in figure 9) where a stable two-torus solution P_3 (a modulated rotating wave) coexists with the two unstable rotating waves P_1 and P_2. This is a mixed mode between the two rotating waves.

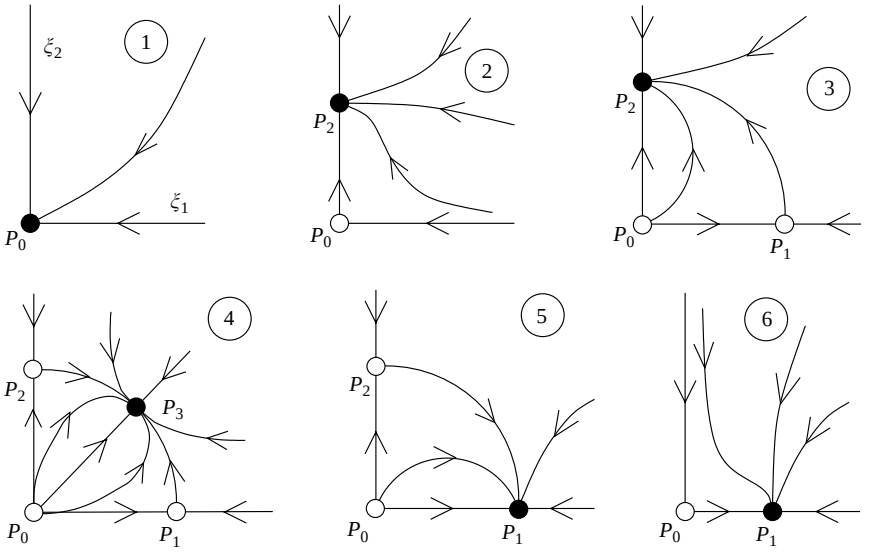

FIGURE 10. Phase portraits corresponding to the six different regions of the double Hopf bifurcation of simple type II in figure 9. Solid (open) circles are stable (unstable) states.

5.1. *Numerical results*

The double Hopf bifurcation is localized by the intersection of the two Hopf bifurcation curves, H_1 and H_2, at which RW$_1$ and RW$_2$ bifurcate from the basic state, respectively. Parts of these Hopf curves are straightforward to determine, the parts which are the first bifurcation curves crossed from the stable basic state. To determine the parts where they are the second bifurcations from the basic state, we compute in appropriate subspaces such that these are primary bifurcations in the respective subspaces. To determine H_2, we compute in an even azimuthal subspace (i.e. all odd azimuthal Fourier modes set to zero), as RW$_1$ does not exist in this subspace. To determine H_1, we compute in an even z-parity subspace, as RW$_2$ has odd z-parity and so does not exist in this subspace. Figure 11 shows the loci of H_1 and H_2 in (Γ, Re) space, indicating that the double Hopf point is ($\Gamma = 1.0264$, $Re = 1949.07$).

In order to determine the Neimark–Sacker curve N_1, at which the even z-parity RW$_1$ loses stability to MRW with odd z-parity that arises due to the growth of the $m = 2$ azimuthal component, we monitor a parity parameter:

$$L_z^2 = \sum_{i=0}^{N_r} \left(\sum_{j=0}^{(N_z-1)/2} \left[|u_{i,2j+1,2}|^2 + |v_{i,2j+1,2}|^2 \right] + \sum_{j=0}^{N_z/2} |w_{i,2j,2}|^2 \right), \tag{5.2}$$

where $(u_{i,j,k}, v_{i,j,k}, w_{i,j,k})$ is the ith radial, jth axial, kth ($k = 2$) Fourier complex spectral coefficient of the velocity. This parity parameter is zero for even z-parity solutions (such as the basic state and RW$_1$) and non-zero for solutions that are not of even z-parity (such as RW$_2$ and MRW). The Neimark–Sacker curve N_2, where the odd z-parity RW$_2$ loses stability to MRW with a non-zero $m = 1$ component is more straightforward to determine, simply by monitoring E_1. These Neimark–Sacker curves are also shown in figure 11. The wedge-shaped region between the two Neimark–Sacker curves corresponds to region 4, depicted in figure 9, where MRW exists and is stable.

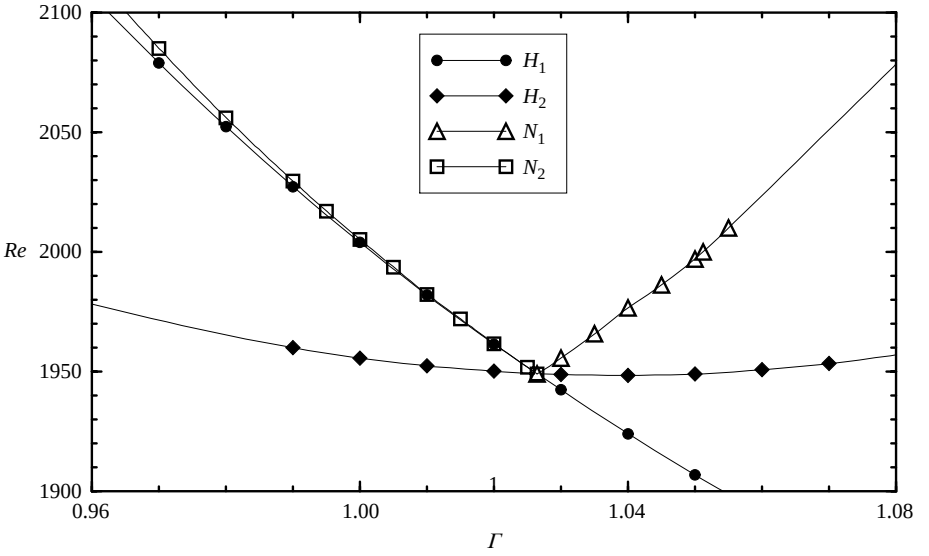

FIGURE 11. Regime diagram in (Γ, Re) space, showing the Hopf bifurcations curves from the basic state to RW_1 (H_1) and to RW_2 (H_2), the Neimark–Sacker curves across which RW_1 and RW_2 become unstable (N_1 and N_2, respectively), leading to the stable mixed mode MRW. In all cases, the bifurcations are supercritical with increasing Re. The double Hopf point is the codimension-2 point where all the curves meet.

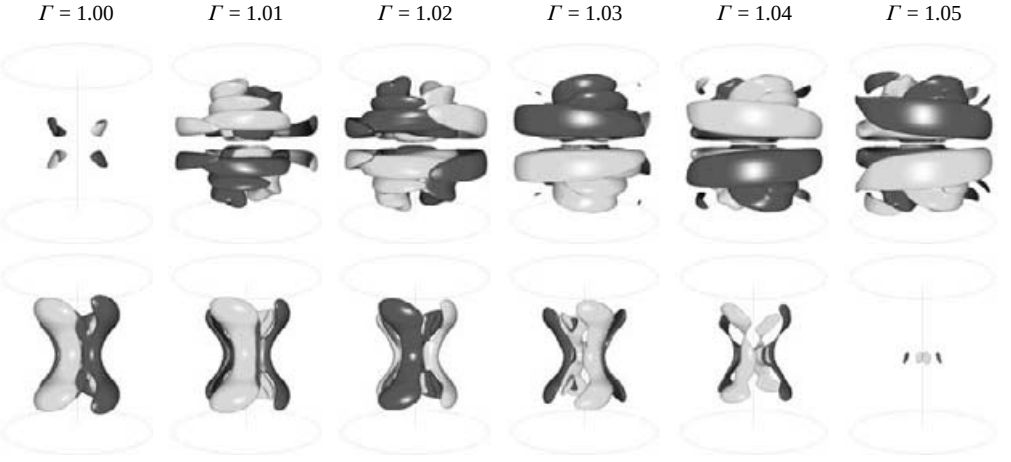

FIGURE 12. Isosurfaces of the $m=1$ (top row) and $m=2$ (bottom row) Fourier components of the axial velocity of MRW at $Re=2010$, for Γ as indicated; all isolevels at ± 0.003.

Figure 12 shows isosurfaces of the $m=1$ (top row) and $m=2$ (bottom row) Fourier components of the axial velocity of MRW at $Re=2010$, for a range of Γ between the two Neimark–Sacker curves N_1 and N_2. As N_2 is crossed with increasing Γ (keeping $Re=2010$ fixed, for example), RW_2 (with odd z-parity) becomes unstable and the stable MRW is spawned. At $\Gamma=1.0$, the $m=2$ component of MRW is virtually identical to that of RW_2 (compare with figure 5), and the $m=1$ component is quite weak, but clearly has even z-parity (the z-component of an even z-parity vector quantity is odd). With increasing Γ, the $m=1$ component of MRW increases in magnitude, and

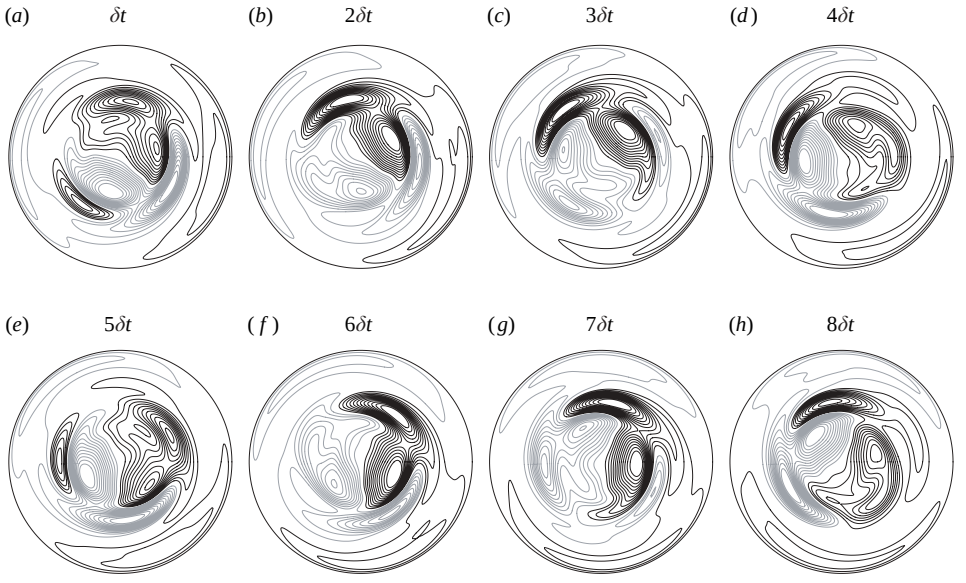

FIGURE 13. Contours of the axial velocity perturbation (i.e. the axial velocity minus its axisymmetric component) of MRW at $Re = 2010$ and $\Gamma = 1.02$ in a horizontal plane at $z = -\Gamma/2$, at 8 instances in time spaced by $\delta t = 1.58$. There are 12 equispaced positive and negative contour levels, in the range ± 0.01.

by $\Gamma = 1.02$ (roughly half-way between the two Neimark–Sacker curves N_1 and N_2 for $Re = 2050$) the magnitude and structure of the $m = 1$ component of MRW is very similar to that of RW_1 (compare with figure 8). The magnitude of the $m = 2$ component of MRW decreases with increasing Γ (but it retains the same spatial structure), and as N_1 is approached (e.g. near $\Gamma = 1.05$), this component vanishes and MRW is absorbed in the Neimark–Sacker bifurcation that results in stabilizing RW_1. In essence, the mixed mode MRW is a combination of RW_1 and RW_2, weighted by the relative distance to N_1 and N_2 (see (A 23)).

Figure 13 shows the temporal evolution of the axial velocity perturbation (i.e. the axial velocity minus its axisymmetric component) of MRW at $Re = 2010$ and $\Gamma = 1.02$ in a horizontal plane at $z = -\Gamma/2$. It is clear that MRW is not simply a linear superposition of RW_1 and RW_2, but has a complex spatial and temporal structure. Nevertheless, the figure shows that on average, the flow structures close to the axis tend to rotate counterclockwise while those near the cylinder wall rotate clockwise. Although these solutions are unstable in the presence of the MRW, they can be computed easily by time evolution in the appropriate invariant subspace: RW_1 is Z_2-invariant, and is stable in the subspace of Z_2-invariant velocity fields; RW_2 exists and is stable in the even Fourier subspace, containing only the even Fourier modes in the azimuthal direction.

Contours of the axial velocity perturbation (i.e. the axial velocity minus its axisymmetric component) of RW_1 and RW_2 at $Re = 1960$ and $\Gamma = 1.025$ in a horizontal plane at $z = -\Gamma/2$ (inside region 4, where the stable state is MRW) are shown in figure 14. As we are very close to the double Hopf bifurcation point, the dominant Fourier mode almost coincides with the corresponding eigenfunction at the double Hopf bifurcation point. The maxima in magnitude of the eigenmode for both RW_1 and RW_2 are comparable and occur for $r \sim 0.5$. The RW_1 eigenmode has a significant

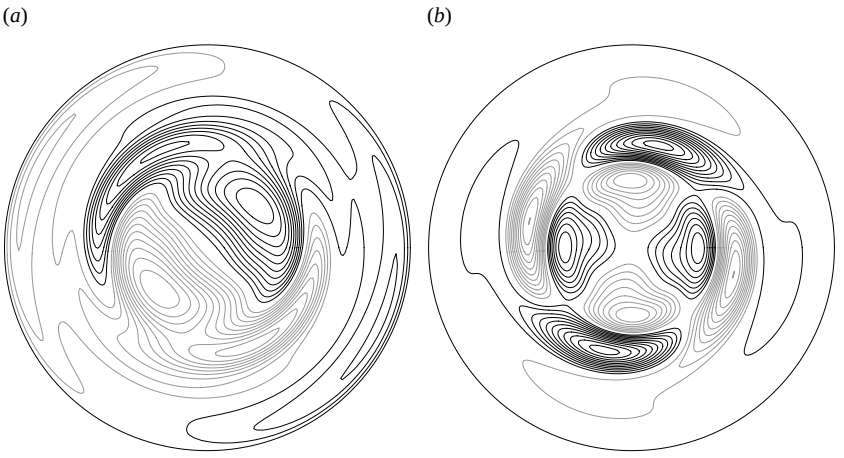

FIGURE 14. Contours of the axial velocity perturbation (i.e. the axial velocity minus its axisymmetric component) of (*a*) RW$_1$ and (*b*) RW$_2$ at $Re = 1960$ and $\Gamma = 1.025$ in a horizontal plane at $z = -\Gamma/2$. There are 12 equispaced positive and negative contour levels, in the range ± 0.03

component near the sidewall ($r = 1$), whereas for RW$_2$ the eigenmode vanishes near the cylinder wall.

The precession periods for RW$_1$ and RW$_2$ at $Re = 1960$ and $\Gamma = 1.025$ are $T_1 = 44.6$ for RW$_1$ and $T_2 = 8.85$ for RW$_2$; RW$_1$ precesses clockwise (retrograde with the endwalls) and RW$_2$ precesses anticlockwise (prograde with the endwalls). The corresponding frequencies are $\omega_1 = -2\pi/T_1 = -0.141$ and $\omega_2 = 2\pi/T_2 = 0.710$. Since ω_1 and ω_2 have opposite sign, the double Hopf bifurcation is non-resonant (see the Appendix). The precession frequencies are given by ω_m/m, where m is the azimuthal wavenumber.

The retrograde precession of RW$_1$ with its eigenmode large near the cylinder wall and the prograde precession of RW$_2$ with its eigenmode vanishing near the cylinder wall, and both eigenmodes having comparable magnitudes for $r \lesssim 0.5$ but with RW$_2$ precessing about 5 times faster than RW$_1$ (in the opposite direction), is consistent with the observed spatiotemporal structure of the mixed-mode MRW (figure 13). From the Appendix, we see that when viewed in an appropriate rotating frame (with rotation frequency ω_1), MRW is seen as a periodic solution with period $T_r = 2\pi/(\omega_2 - 2\omega_1) = 2\pi/[0.710 - 2(-0.141)] = 6.33$. The frames in figure 13 are shown at phases approximately one quarter of a period apart ($\delta t = 1.58$, the approximation is necessary owing to the discrete time step used in the computations). Comparing frames $4\delta t \approx T_r$ apart we see that the structure is unchanged, but has been rotated by $\omega_1 T_r = 0.9004$ rad.

6. Physical mechanisms

It is tempting to try and extract the physical mechanisms responsible for flow instability in complicated flows by isolating and idealizing certain flow features of the unstable basic flow state, and then do a classical stability analysis on these. This approach works reasonably well when the flow feature in question is well isolated. For example, in the flow studied in this paper, the boundary layers on the rotating endwalls are very well described by von Kármán's similarity solution for the boundary layer on a rotating disk (von Kármán 1921). This self-similar solution described the

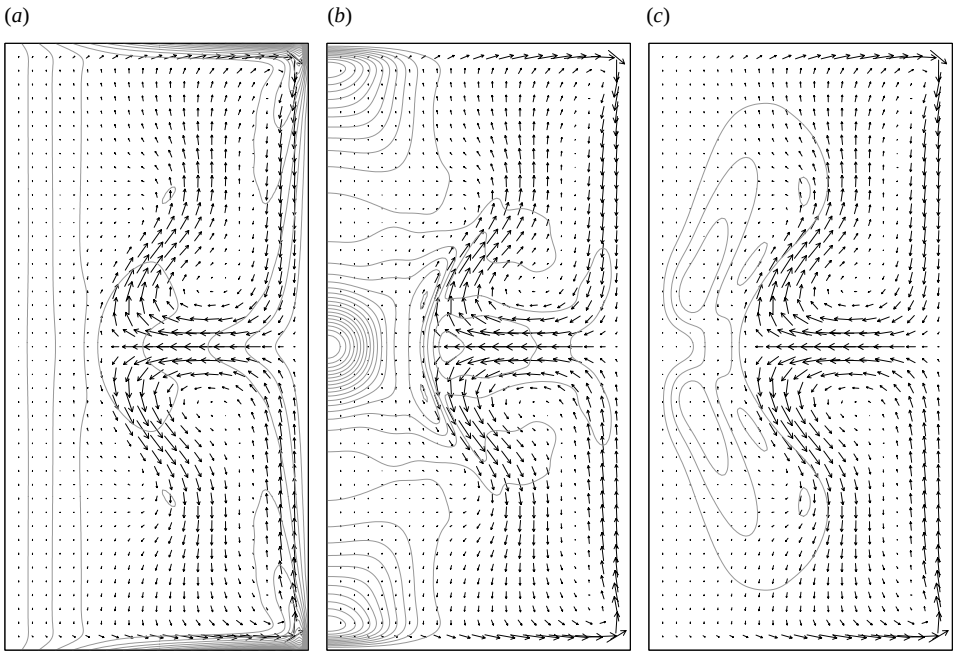

FIGURE 15. Contours of the modal energy density for (*a*) e_0 of the basic state, (*b*) e_1 of RW$_1$, and (*c*) e_2 of RW$_2$, all at $Re = 2050$, $\Gamma = 1.0$. On all three, the arrows are the (u, w) velocity vectors of the basic state in the meridional plane. For (*a*) the 18 contours are quadratically space over [0,], for (*b*) and (*c*) they are linearly spaced over $[0, 2.8 \times 10^{-4}]$.

boundary-layer flow in the enclosed cylinder for $r \leqslant 0.95$. Stability analysis of such disk flows (e.g. Gregory, Stuart & Walker 1955) shows that for the *Re* values considered in this paper, the boundary-layer flow is stable, in accord with our numerical solutions. On the other hand, conducting a similar analysis on the region of solid-body rotation ($r < 0.2$, $z \in [-\Gamma/2, \Gamma/2]$) gives absolute stability for all *Re* (e.g. Joseph 1976), and yet, as we shall now demonstrate for $Re \sim 2000$, the region of solid-body rotation is not stable.

The usual way to determine the instability mechanisms is to look at the characteristics of the eigenmode responsible for the instability. The eigenmodes for RW$_1$ and RW$_2$, and their symmetries have already been described in the earlier sections. Here we determine what features of the base state are associated with the maximum kinetic energy of the eigenmodes. Figure 15(*a*) shows contours of the kinetic energy of the base flow, e_0, together with meridional (u, v) velocity vectors of the base flow. The kinetic energy is mainly concentrated in the endwall boundary layers; the contours are quadratically spaced so that several contour levels are concentrated near 0, thereby letting us see where the flow is most energetic outside of the boundary layers: in the jet-shear-layer at the mid-plane, and in the resulting rebound region following the impact with the solid-body-rotation region. In these regions, the meridional velocities (u, v) of the base state also reach local maxima.

Figures 15(*b*) and 15(*c*) show equispaced contours of kinetic energy for the RW$_1$ and RW$_2$ eigenmodes. The kinetic energy contours of RW$_1$ (figure 15*b*) show the maximum at the cylinder axis ($r = 0, z = 0$), where the axisymmetric jet of the base flow converges towards; there are also some secondary maxima located where the jet collides with the solid-body-rotation region. Other maxima appear in the

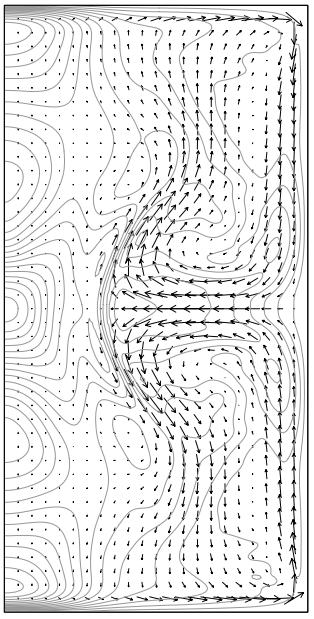

FIGURE 16. Contours of the modal energy density for MRW (all Fourier modes except $m = 0$), at $Re = 2050$, $\Gamma = 1.0$. The 18 contours levels are linearly spaced over $[0, 2.8 \times 10^{-4}]$.

solid-body-rotation region near the endwalls. From the kinetic energy contours and the three-dimensional isosurface plots of the eigenmode (figure 8), it is seen that this mode produces a non-axisymmetric deformation of the solid-body-rotation region and of the jet, as a result of their collision. The kinetic energy contours of RW_2 eigenmode (figure 15*c*) show that the energy of the perturbation is located on the inner side of the rebounding jet, as can also be seen in the three-dimensional isosurface plots of the eigenmode (figure 5). In this mode, neither the solid-body-rotation region nor the jet-shear-layer are deformed, except in a small neighbourhood of the impact region. This mode only produces a non-axisymmetric deformation of the rebounding fluid.

In the (Re,Γ) parameter regime where the mixed mode MRW exists and is stable (see figure 11), neither RW_1 nor RW_2 are stable. Figure 16 shows the kinetic energy of MRW minus the kinetic energy corresponding to its axisymmetric component, which is essentially a combination of e_1 and e_2 from RW_1 and RW_2 (this was also essentially shown in figure 12), so that the physical mechanisms for MRW are a mix of both the core/jet deformation and the rebound deformation. For $\Gamma > 1$, the core/jet deformation mechanism dominates and for $\Gamma < 1$, the rebound deformation dominates. This is understood in terms of the robustness of the solid-body-rotation core region, which is extensive for $\Gamma < 1$ (Lopez *et al.* 2004), and so the collision with the jet does not deform it. For $\Gamma > 1$, the radial extent of the solid-body-rotation core region is much smaller and it is more feeble and subject to large deformation by the jet impingement.

7. Conclusion

Cylinder flows with rotating endwalls have been widely studied; these systems have $SO(2)$ symmetry (invariance to rotations about the axis) which may or may not be broken in various parameter regimes. Here, we have studied the case where

both endwalls co-rotate, giving the system an additional Z_2 symmetry – reflection about the cylinder half-height. We have analysed the bifurcations of the $SO(2) \times Z_2$ basic state (axisymmetric and reflection symmetric), which lead to (non-axisymmetric) rotating wave states as primary modes of instability that may or may not be reflection symmetric. Cylinder flows with one rotating endwall and a free surface have often been modelled by employing a flat stress-free interface. This model is equivalent to imposing Z_2 symmetry at the mid-plane in the extended system we have studied.

We have shown that for aspect ratios $\Gamma > 1$, the primary bifurcation preserves Z_2. This is in agreement with deep free-surface experiments (Hirsa *et al.* 2002), and justifies the use of the idealized flat stress-free interface model for these deep systems. However, when $\Gamma < 1$, we have observed that the primary bifurcation breaks Z_2. For these shallow systems, the experiments do not agree with results imposing Z_2; instead, the experimental flows in the bulk closely resemble computed flows with broken Z_2 symmetry (Miraghaie *et al.* 2003).

Here, we have explored in detail the spatiotemporal dynamics in the region with $\Gamma \sim 1$, where Z_2-symmetry preserving and Z_2-symmetry breaking instability modes compete. In this region, the pure modes (rotating waves) are not stable, and the only stable state is a mixed mode (a quasi-periodic modulated rotating wave) possessing characteristics of both pure modes. This is in contrast to the usual scenarios following symmetry breaking (e.g. via steady pitchfork bifurcations) that result in multiple stable states; common examples include Taylor–Couette flows (Coles 1965) and Rayleigh–Bénard convection (Mullin 1999). Two physical instability mechanisms are responsible for the symmetry-breaking bifurcations in our problem. The basic state consists of a region of essentially solid-body rotation for $r \lesssim 0.2$ and overturning meridional swirling flow for $r \gtrsim 0.2$ which supports a swirling jet at the mid-plane. As this jet impinges on the region of solid-body rotation, the flow is subjected to two symmetry-breaking types of deformation; both break the axisymmetry, but only one breaks the reflection symmetry. The mode that only breaks $SO(2)$ is the core/jet deformation mode, and the other is the rebound deformation mode. For $\Gamma \sim 1$, these two mechanisms compete, and the result of this competition is a mixed mode that exhibits the consequences of both instability mechanisms. By computing in appropriate subspaces, the details of the individual instability mechanisms have been explored and compared with the details of the mixed mode. Our analysis of the problem is from a flow physics point of view as well as from a bifurcation theory with symmetry point of view. The theory provides precise predictions of the spatiotemporal characteristics of the various states, and these are in full agreement with the nonlinear Navier–Stokes solutions.

This work was partially supported by NSF grant CTS-9908599 (USA) and MCYT grant BFM2001-2350 (Spain). Part of this work was completed during visits by both authors to ETH Zürich with support from Swiss NSF grant P1012-100371.

Appendix. Normal form of the double Hopf bifurcation with $SO(2) \times Z_2$ symmetry

The technique of Iooss & Adelmeyer (1998), which provides a clear and simple method to obtain normal forms, incorporating symmetry considerations, is now used for the double Hopf bifurcation with the $SO(2) \times Z_2$ symmetry group. In the codimension-1 Hopf bifurcation, the presence of $SO(2) \times Z_2$ symmetry does not alter the generic normal form, and the same is true for the double Hopf bifurcation

without resonance. However, it is important to specify what the resonance conditions are, because as we shall see, $SO(2) \times Z_2$ inhibits resonance. Resonance is only possible if both the temporal frequencies (imaginary parts of the eigenvalues at the bifurcation point, ω_1^0 and ω_2^0) and the spatial frequencies (azimuthal wavenumbers, m_1 and m_2) satisfy the resonance condition $\omega_2^0/\omega_1^0 = m_2/m_1 = p/q$, where p and q are positive irreducible integers. Additional restrictions on the normal form may appear, depending on how the Z_2 symmetry acts on the eigenvectors, and this is governed by the z-parities, s_1 and s_2. We will follow closely the analysis of the double Hopf bifurcation with $SO(2)$ symmetry in Marques *et al.* (2002).

The normal form theorem says that the dynamical system in a neighbourhood of the fixed point (steady, axisymmetric basic state) in the centre manifold can be cast in the form

$$\dot{z}_i = \mathrm{i}\omega_i^0 z_i + P_i(z_1, z_2, \overline{z}_1, \overline{z}_2, \mu), \tag{A 1}$$

plus complex conjugate, for $i = 1, 2$. The functions P_i are second order in z for $\mu = 0$ and satisfy

$$P(\exp(tL_o^*)z) = \exp(tL_o^*)P(z), \tag{A 2}$$

$$P(R_\beta z) = R_\beta P(z), \tag{A 3}$$

$$P(Kz) = KP(z), \tag{A 4}$$

where L_o is the linear part of the dynamical system at criticality and L_o^* is the corresponding adjoint operator. We have used vector notation $z = (z_1, z_2, \overline{z}_1, \overline{z}_2)$ and $P = (P_1, P_2, \overline{P}_1, \overline{P}_2)$ in order to keep the expressions compact. In this notation, the matrices $\mathrm{e}^{tL_o^*}$, R_β and K are diagonal:

$$\mathrm{e}^{tL_o^*} = \mathrm{diag}\big(\exp(-\mathrm{i}\omega_1^0 t), \exp(-\mathrm{i}\omega_2^0 t), \exp(\mathrm{i}\omega_1^0 t), \exp(\mathrm{i}\omega_2^0 t)\big), \tag{A 5}$$

$$R_\beta = \mathrm{diag}\big(\exp(\mathrm{i}m_1\beta), \exp(\mathrm{i}m_2\beta), \exp(-\mathrm{i}m_1\beta), \exp(-\mathrm{i}m_2\beta)\big), \tag{A 6}$$

$$K = \mathrm{diag}(s_1, s_2, s_1, s_2). \tag{A 7}$$

Equation (A 2) gives the simplest form of P attainable using the structure of the linear part L_o, and (A 3) and (A 4) give the additional constraints on P imposed by the symmetries $SO(2)$ and Z_2, respectively.

Let $z_1^{k_1} z_2^{k_2} \overline{z}_1^{l_1} \overline{z}_2^{l_2}$ be an admissible monomial in P_1; it must satisfy (A 2), (A 3) and (A 4), i.e.

$$(k_1 - l_1 - 1)\omega_1^0 + (k_2 - l_2)\omega_2^0 = 0, \tag{A 8}$$

$$(k_1 - l_1 - 1)m_1 + (k_2 - l_2)m_2 = 0, \tag{A 9}$$

$$s_1^{k_1 - l_1 - 1} s_2^{k_2 - l_2} = 1. \tag{A 10}$$

If $\omega_2^0/\omega_1^0 \notin \mathbb{Q}$, the non-resonant case, the only solution to (A 8) is $k_1 = l_1 + 1$ and $k_2 = l_2$, and (A 9) and (A 10) are identically satisfied. The symmetry group $SO(2) \times Z_2$ does not alter the normal form, except in the case of resonance. The non-resonant normal form is

$$P_1 = z_1 Q_1, \quad P_2 = z_2 Q_2, \tag{A 11}$$

where $Q_i(|z_1|^2, |z_2|^2)$, which coincides with the generic case analysed in Kuznetsov (1998).

If $\omega_2^0/\omega_1^0 = p/q \in \mathbb{Q}$, we are in the temporal resonant case and (A 8) admits additional solutions:

$$k_1 - l_1 - 1 = kp, \quad k_2 - l_2 = -kq, \quad k \in \mathbb{Z}, \tag{A 12}$$

and additional monomials $z_1(z_1^p\bar{z}_2^q)^j|z_1|^{2r}|z_2|^{2l}$, $j \in \mathbb{Z}$, appear in the normal form. If ω_1^0 and ω_2^0 have the same sign, we can take p and q positive, and we obtain

$$P_1 = z_1 Q_{11} + \bar{z}_1^{p-1} z_2^q Q_{12}, \tag{A 13}$$

$$P_2 = z_2 Q_{21} + z_1^p \bar{z}_2^{q-1} Q_{22}, \tag{A 14}$$

where $Q_{ii}(|z_1|^2, |z_2|^2, z_1^p\bar{z}_2^q)$, $i = 1, 2$, and $Q_{ij}(|z_1|^2, |z_2|^2, \bar{z}_1^p z_2^q)$, $i \neq j$. If ω_1^0 and ω_2^0 have opposite signs, then either p or q must be negative; we can take $p < 0$. In this case, P_1 and P_2 can be written as

$$P_1 = z_1 Q_{11} + \bar{z}_1^{|p|-1}\bar{z}_2^q Q_{12}, \tag{A 15}$$

$$P_2 = z_2 Q_{21} + \bar{z}_1^{|p|}\bar{z}_2^{q-1} Q_{22}, \tag{A 16}$$

where $Q_{i1}(|z_1|^2, |z_2|^2, z_1^{|p|}z_2^q)$, and $Q_{i2}(|z_1|^2, |z_2|^2, \bar{z}_1^{|p|}\bar{z}_2^q)$, $i \neq j$.

Now we determine whether (A 12) is consistent with (A 9) and (A 10). If $m_1 = m_2 = 0$, (A 9) is identically zero, the centre manifold lies in an $SO(2)$-equivariant subspace, and the symmetry group $SO(2)$ does not play any role in the neighbourhood of the bifurcation. This is the generic non-symmetric resonant case, with normal form (A 13) and (A 14) when ω_1^0 and ω_2^0 have the same sign, or (A 15) and (A 16) when ω_1^0 and ω_2^0 have opposite signs. The symmetry K imposes an additional condition, $(s_1^p s_2^q)^k = 1$ (A 10). When $s_1^p s_2^q = -1$, k must be even, and so the functions Q_{i1} are even and Q_{i2} are odd in their last argument.

If one of the m_i is zero and the other is not, (A 9) implies $k_1 = l_1 + 1$ and $k_2 = l_2$, the resonant terms are suppressed by the presence of the symmetry, and the normal form is (A 11). If both m_i are non-zero, the resonant terms (A 12) must satisfy (A 9) and (A 10), which gives $m_2\omega_1^0 - m_1\omega_2^0 = 0$ and $(s_1^p s_2^q)^k = 1$. Again, the presence of $SO(2)$ inhibits resonance and the normal form is (A 11), except when the spatial and temporal modes satisfy the same resonance condition $\omega_2^0/\omega_1^0 = m_2/m_1 = p/q$; notice that this condition can never be satisfied if the two rotating waves do not precess in the same direction. When this simultaneous resonance condition is satisfied, the normal form is (A 13)–(A 14), with some additional restrictions imposed by $(s_1^p s_2^q)^k = 1$: the functions Q_{i1} are even and Q_{i2} are odd in their last argument.

Substituting (A 11) into (A 1), we obtain the normal form in the non-resonant case:

$$\dot{z}_i = z_i\left[\mathrm{i}\omega_i^0 + Q_i(|z_1|^2, |z_2|^2)\right]. \tag{A 17}$$

In terms of the moduli and phases of z_i, $z_i = r_i \exp(\mathrm{i}\phi_i)$, we have

$$\dot{r}_i = r_i Q_i^R\left(r_1^2, r_2^2\right), \tag{A 18}$$

$$\dot{\phi}_i = \omega_i^0 + Q_i^I\left(r_1^2, r_2^2\right), \tag{A 19}$$

where Q_i^R and Q_i^I are the real and imaginary parts of Q_i, respectively. Up to fourth order in r_1 and r_2, and assuming that the coefficients of second order in Q_i^R are non-zero, the normal form can be written as (Kuznetsov 1998):

$$\left.\begin{aligned}
\dot{r}_1 &= r_1\left(\mu_1 + p_{11}r_1^2 + p_{12}r_2^2 + q_1 r_2^4\right),\\
\dot{r}_2 &= r_2\left(\mu_2 + p_{21}r_1^2 + p_{22}r_2^2 + q_2 r_1^4\right),\\
\dot{\phi}_1 &= \omega_1^0 + \psi_1(r_1, r_2, \mu_1, \mu_2),\\
\dot{\phi}_2 &= \omega_2^0 + \psi_2(r_1, r_2, \mu_1, \mu_2),
\end{aligned}\right\} \tag{A 20}$$

where we have introduced explicitly the normalized bifurcation parameters μ_1 and μ_2. The dynamics of the moduli r_1 and r_2 decouple from the phase dynamics, and we end up with an effective two-dimensional normal form for r_1 and r_2.

This effective normal form has four fixed points, that after introducing the phase dependence, become one fixed point, two periodic solutions, and a quasi-periodic solution. The stability and regions of existence of these solutions depend on the values of p_{ij} and q_i. There are eleven different scenarios, classified in two categories: simple ($p_{11}p_{22} > 0$) and difficult ($p_{11}p_{22} < 0$). For a specific problem, in order to determine the corresponding scenario, there are two options. One option is to compute the normal form coefficients p_{ij} and q_i using the eigenvectors at the bifurcation point, which is very complicated in the present case. The other option is to compute numerically a regime diagram in parameter space, delineating the regions of existence of the solutions, and determine their stability in a neighbourhood of the double Hopf bifurcation point, and use this information to determine the corresponding scenario; this is the approach we have employed here. Figure 11 is the regime diagram we have obtained, by computing a few hundred solutions for different parameter values close to the double Hopf bifurcation point. There are only two double Hopf scenarios compatible with our results, and they are types I and II of the simple case (Kuznetsov 1998). They differ in the stability of the quasi-periodic solution. As in our case the quasi-periodic solution is stable, we conclude that our problem corresponds to the simple case, type II scenario. We describe this scenario in detail in § 5.

For the simple cases ($p_{11}p_{22} > 0$), the fourth-order terms in (A 20) can be neglected. Introducing new variables, $\xi_1 = -p_{11}r_1^2$ and $\xi_2 = -p_{22}r_2^2$, we obtain

$$\left.\begin{aligned} \dot{\xi}_1 &= 2\xi_1(\mu_1 - \xi_1 - \theta\xi_2), \\ \dot{\xi}_2 &= 2\xi_2(\mu_2 - \delta\xi_1 - \xi_2), \end{aligned}\right\} \tag{A 21}$$

where $\theta = p_{12}/p_{22}$ and $\delta = p_{21}/p_{11}$. In our problem $\theta > 0$, $\delta > 0$ and $\theta\delta < 1$. This normal form admits up to four fixed points:

$$P_0 = (0, 0), \quad P_1 = (\mu_1, 0), \quad P_2 = (0, \mu_2), \tag{A 22}$$

$$P_3 = \left(\frac{\mu_1 - \theta\mu_2}{1 - \theta\delta}, \frac{\mu_2 - \delta\mu_1}{1 - \theta\delta}\right). \tag{A 23}$$

P_0 exists for all values of μ_1 and μ_2, and is stable for $\mu_1, \mu_2 < 0$. This corresponds to our basic state. P_1 exists for $\mu_1 > 0$ and is stable for $\mu_2 < \delta\mu_1$ (below the N_1 curve in figure 9); P_2 exists for $\mu_2 > 0$ and is stable for $\mu_2 > \theta^{-1}\mu_1$ (above the N_2 curve in figure 9). By including the phase information, P_1 and P_2 are limit cycles, corresponding to our RW_1 and RW_2. P_3 exists and is stable between N_1 and N_2. As both moduli are non-zero for P_3, by including the phase information, it is recognized as a quasi-periodic solution on a two-torus, and in our case it corresponds to MRW. For P_1, P_2 and P_3, r_1 and r_2 are constant, and so they have constant angular frequencies:

$$\left.\begin{aligned} \omega_1 &= \dot{\phi}_1 = \omega_1^0 + \psi_1(r_1, r_2, \mu_1, \mu_2), \\ \omega_2 &= \dot{\phi}_2 = \omega_2^0 + \psi_2(r_1, r_2, \mu_1, \mu_2). \end{aligned}\right\} \tag{A 24}$$

In the non-resonant case, we have seen that the normal form is unaltered by the symmetry group $\mathscr{G}$. Nevertheless, the symmetries act on the bifurcating solutions in a well-determined fashion. From (A 6) and (A 7), we see that the action of $\mathscr{G}$ leaves the moduli (r_1, r_2) invariant, and $\mathscr{G}$ acts only on the phases (ϕ_1, ϕ_2). The action of $\mathscr{G}$ on

the phases is:

$$R_\beta \begin{pmatrix} \phi_1 \\ \phi_2 \end{pmatrix} = \begin{pmatrix} \phi_1 + m_1\beta \\ \phi_2 + m_2\beta \end{pmatrix}, \tag{A 25}$$

$$K \begin{pmatrix} \phi_1 \\ \phi_2 \end{pmatrix} = \begin{pmatrix} \phi_1 + (1-s_1)\pi/2 \\ \phi_2 + (1-s_2)\pi/2 \end{pmatrix}. \tag{A 26}$$

In our problem, $m_1 = 1$, $s_1 = 1$, $m_2 = 2$, and $s_2 = -1$, and the action of $\mathscr{G}$ on the phases is simply:

$$R_\beta \begin{pmatrix} \phi_1 \\ \phi_2 \end{pmatrix} = \begin{pmatrix} \phi_1 + \beta \\ \phi_2 + 2\beta \end{pmatrix}, \tag{A 27}$$

$$K \begin{pmatrix} \phi_1 \\ \phi_2 \end{pmatrix} = \begin{pmatrix} \phi_1 \\ \phi_2 + \pi \end{pmatrix}. \tag{A 28}$$

The basic state P_0 is a steady solution, it has no phase, and hence it is $\mathscr{G}$-invariant. The rotating wave P_1 has $r_2 = 0$ and so we only need to consider ϕ_1; P_1 is K-invariant but R_β (as a spatial symmetry) is broken, and the action of R_β is equivalent to a time translation $\tau : \phi_1 \to \phi_1 + \omega_1\tau = \phi_1 + \beta$, i.e. $\tau = \beta/\omega_1$, i.e. R_β becomes a spatiotemporal symmetry. The limit cycle as a set is $\mathscr{G}$-invariant, but it is only pointwise invariant to K.

The rotating wave P_2 has $r_1 = 0$ and so we only need to consider ϕ_2; both K and R_β are broken (as spatial symmetries), and their actions are equivalent to time translations (they become spatiotemporal symmetries):

$$R_\beta : \phi_2 \to \phi_2 + \omega_2\tau_1 = \phi_2 + 2\beta, \quad \tau_1 = 2\beta/\omega_2, \tag{A 29}$$

$$K : \phi_2 \to \phi_2 + \omega_2\tau_2 = \phi_2 + \pi, \quad \tau_2 = \pi/\omega_2. \tag{A 30}$$

When $\beta = \pi/2$, the actions of R_β and K are equivalent, and their combined action leaves the phase ϕ_2 unchanged. The combination $KR_{\pi/2}$ is a spatial symmetry of P_2; this combination generates the spatial symmetry group $\Delta = Z_4$. The limit cycle as a set is $\mathscr{G}$-invariant, but it is only pointwise invariant to Z_4.

P_3 is actually a family of quasi-periodic solutions that generates a two-torus. From an individual P_3 solution, the whole family is generated by applying R_β, $\beta \in [0, 2\pi)$. The two-torus as a set is $\mathscr{G}$-invariant, but the individual P_3 solutions do not retain any pointwise (spatial) symmetry. The time evolution of a P_3 solution on the two-torus is given by

$$\Phi_t \begin{pmatrix} \phi_1 \\ \phi_2 \end{pmatrix} = \begin{pmatrix} \phi_1 + \omega_1 t \\ \phi_2 + \omega_2 t \end{pmatrix}, \tag{A 31}$$

where Φ_t is the time evolution operator acting on the phases ϕ_1 and ϕ_2. As ω_1 and ω_2 are incommensurate, P_3 is quasi-periodic. However, in an appropriate rotating frame of reference, it becomes a periodic solution; using (A 25), in an arbitrary reference frame rotating with angular velocity ω_r, the time evolution of P_3 is given by:

$$R_{-\omega_r t}\Phi_t \begin{pmatrix} \phi_1 \\ \phi_2 \end{pmatrix} = \begin{pmatrix} \phi_1 + (\omega_1 - m_1\omega_r)t \\ \phi_2 + (\omega_2 - m_2\omega_r)t \end{pmatrix}. \tag{A 32}$$

When ω_r is such that $(\omega_1 - m_1\omega_r)/(\omega_2 - m_2\omega_r)$ is rational, P_3 is periodic in the rotating reference frame. The two simplest choices are $\omega_r = \omega_i/m_i$, for $i = 1$ and 2. These choices are precisely the precession frequencies of the pure modes P_1 and P_2.

In the particular problem considered in this paper, the action of K on the phase ϕ_1, (A 27) and (A 28), is trivial. Viewing P_3 in the frame of reference rotating with $\omega_r = \omega_1$, the action of K and temporal evolution on ϕ_2 are:

$$K\phi_2 = \phi_2 + \pi; \qquad \Phi_t\phi_2 = \phi_2 + (\omega_2 - 2\omega_1)t. \tag{A 33}$$

Hence, P_3 (a periodic solution in the rotating frame with period $2\pi/(\omega_2 - 2\omega_1)$) has a spatiotemporal symmetry consisting of the reflection K composed of a half-period time evolution. This symmetry generates the group Z_2, which is a spatiotemporal involution here.

REFERENCES

Armbruster, D., Guckenheimer, J. & Holmes, P. 1988 Heteroclinic cycles and modulated travelling waves in systems with $O(2)$ symmetry. *Physica* D **29**, 257–282.

Benjamin, T. B. 1978 Bifurcation phenomena in steady flows of a viscous fluid. *Proc. R. Soc. Lond.* A **359**, 1–26.

Benjamin, T. B. & Mullin, T. 1981 Anomalous modes in the Taylor experiment. *Proc. R. Soc. Lond.* A **377**, 221–249.

Brons, M., Voigt, L. K. & Sorensen, J. N. 1999 Streamline topology of steady axisymmetric vortex breakdown in a cylinder with co- and counter-rotating end-covers. *J. Fluid Mech.* **401**, 275–292.

Brons, M., Voigt, L. K. & Sorensen, J. N. 2001 Topology of vortex breakdown bubbles in a cylinder with a rotating bottom and a free surface. *J. Fluid Mech.* **428**, 133–148.

Brown, G. L. & Lopez, J. M. 1990 Axisymmetric vortex breakdown. Part 2. Physical mechanisms. *J. Fluid Mech.* **221**, 553–576.

Cliffe, K. A., Kobine, J. J. & Mullin, T. 1992 The role of anomalous modes in Taylor–Couette flow. *Phil. Trans. Roy. Soc. Lond.* A **439**, 341–357.

Cliffe, K. A. & Mullin, T. 1985 A numerical and experimental study of anomalous modes in the Taylor experiment. *J. Fluid Mech.* **153**, 243–258.

Coles, D. 1965 Transition in circular Couette flow. *J. Fluid Mech.* **21**, 385–425.

Gelfgat, A. Y., Bar-Yoseph, P. Z. & Solan, A. 1996 Steady states and oscillatory instability of swirling flow in a cylinder with rotating top and bottom. *Phys. Fluids* **8**, 2614–2625.

Goldstein, H. F., Knobloch, E., Mercader, I. & Net, M. 1993 Convection in a rotating cylinder. Part 1. Linear theory for moderate Prandtl numbers. *J. Fluid Mech.* **248**, 583–604.

Goldstein, H. F., Knobloch, E., Mercader, I. & Net, M. 1994 Convection in a rotating cylinder. Part 2. Linear theory for low Prandtl numbers. *J. Fluid Mech.* **262**, 293–324.

Golubitsky, M., Stewart, I. & Schaeffer, D. G. 1988 *Singularities and Groups in Bifurcation Theory*, vol 2. Springer.

Gregory, H. N., Stuart, J. T. & Walker, W. S. 1955 On the stability of three dimensional boundary layers with application to the flow due to a rotating disk. *Phil. Trans. Roy. Soc. Lond.* A **248**, 155–199.

Guckenheimer, J. & Holmes, P. 1997 *Nonlinear Oscillations, Dynamical Systems, and Bifurcations of Vector Fields*. Springer.

Hirsa, A. H., Lopez, J. M. & Miraghaie, R. 2002 Symmetry breaking to a rotating wave in a lid-driven cylinder with a free surface: experimental observation. *Phys. Fluids* **14**, L29–L32.

Iooss, G. & Adelmeyer, M. 1998 *Topics in Bifurcation Theory and Applications*, 2nd edn. World Scientific.

Joseph, D. D. 1976 *Stability of Fluid Motions I*. Springer.

von Kármán, T. 1921 Über laminare und turbulente Reibung. *Z. Angew. Math. Mech.* **1**, 2605–2613.

Kuznetsov, Y. A. 1998 *Elements of Applied Bifurcation Theory*, 2nd edn. Springer.

Lamb, J. S. W. & Melbourne, I. 1999 Bifurcation from discrete rotating waves. *Arch. Rat. Mech. Anal.* **149**, 229–270.

Lopez, J. M. 1995 Unsteady swirling flow in an enclosed cylinder with reflectional symmetry. *Phys. Fluids* **7**, 2700–2714.

Lopez, J. M. & Marques, F. 2003 Small aspect ratio Taylor–Couette flow: onset of a very-low-frequency three-torus state. *Phys. Rev.* E **68**, 036302.

Lopez, J. M., Marques, F., Hirsa, A. H. & Miraghaie, R. 2004 Symmetry breaking in free-surface cylinder flows. *J. Fluid Mech.* **502**, 99–126.

Lopez, J. M., Marques, F. & Shen, J. 2002 An efficient spectral-projection method for the Navier–Stokes equations in cylindrical geometries II. Three dimensional cases. *J. Comput. Phys.* **176**, 384–401.

Marques, F., Lopez, J. M. & Shen, J. 2002 Mode interactions in an enclosed swirling flow: a double Hopf bifurcation between azimuthal wavenumbers 0 and 2. *J. Fluid Mech.* **455**, 263–281.

Miraghaie, R., Lopez, J. M. & Hirsa, A. H. 2003 Flow induced patterning at the air/water interface. *Phys. Fluids* **15**, L45–L48.

Mullin, T. 1999 Flow state multiplicity in convection. *Phys. Fluids* **11**, 2815–2817.

Mullin, T., Toya, Y. & Tavener, S. J. 2002 Symmetry breaking and multiplicity of states in small aspect ratio Taylor–Couette flow. *Phys. Fluids* **14**, 2778–2787.

Nore, C., Tuckerman, L. S., Daube, O. & Xin, S. 2003 The 1:2 mode interaction in exactly counter-rotating von Karman swirling flow. *J. Fluid Mech.* **477**, 51–88.

Schulz, A., Pfister, G. & Tavener, S. J. 2003 The effect of outer cylinder rotation on Taylor–Couette flow at small aspect ratio. *Phys. Fluids* **15**, 417–425.

Scott, J. C. 1975 The preparation of water for surface-clean fluid mechanics. *J. Fluid Mech.* **69**, 339–351.

Spohn, A. 1991 Ecoulement et éclatement tourbillonnaires engendrés par un disque tournant dans une enceinte cylindrique. PhD thesis, I'Universite Joseph-Fourier, Grenoble I.

Spohn, A., Mory, M. & Hopfinger, E. J. 1993 Observations of vortex breakdown in an open cylindrical container with a rotating bottom. *Exps. Fluids* **14**, 70–77.

Spohn, A., Mory, M. & Hopfinger, E. J. 1998 Experiments on vortex breakdown in a confined flow generated by a rotating disk. *J. Fluid Mech.* **370**, 73–99.

Valentine, D. T. & Jahnke, C. C. 1994 Flows induced in a cylinder with both end walls rotating. *Phys. Fluids* **6**, 2702–2710.

Young, D. L., Sheen, H. J. & Hwu, T. Y. 1995 Period-doubling route to chaos for a swirling flow in an open cylindrical container with a rotating-disk. *Exps. Fluids* **18**, 389–392.

Zhong, F., Ecke, R. & Steinberg, V. 1991 Asymmetric modes and the transition to vortex structures in rotating Rayleigh–Bénard convection. *Phys. Rev. Lett.* **67**, 2473–2476.